



# Warping Away Gravitational Instabilities in Protoplanetary Discs

Sahl Rowther<sup>1,2</sup> , Rebecca Nealon<sup>1,2</sup> , and Farzana Meru<sup>1,2</sup> <sup>1</sup> Centre for Exoplanets and Habitability, University of Warwick, Coventry, CV4 7AL, UK; [sahl.rowther@warwick.ac.uk](mailto:sahl.rowther@warwick.ac.uk)<sup>2</sup> Department of Physics, University of Warwick, Coventry, CV4 7AL, UK

Received 2021 August 23; revised 2021 November 9; accepted 2021 November 11; published 2022 February 3

## Abstract

We perform three-dimensional smoothed-particle hydrodynamics simulations of warped, non-coplanar gravitationally unstable discs to show that as the warp propagates through the self-gravitating disk, it heats up the disk rendering it gravitationally stable, thus losing their spiral structure and appearing completely axisymmetric. In their youth, protoplanetary discs are expected to be massive and self-gravitating, which results in nonaxisymmetric spiral structures. However recent observations of young protoplanetary discs with the Atacama Large Millimeter/submillimeter Array have revealed that discs with large-scale spiral structure are rarely observed in the midplane. Instead, axisymmetric discs, with some also having ring and gap structures, are more commonly observed. Our work involving warps, non-coplanar disk structures that are expected to commonly occur in young discs, potentially resolves this discrepancy between observations and theoretical predictions. We demonstrate that they are able to suppress the large-scale spiral structure of self-gravitating protoplanetary discs.

*Unified Astronomy Thesaurus concepts:* [Protoplanetary disks \(1300\)](#)

## 1. Introduction

In recent years, a large number of protoplanetary discs have been observed at millimeter wavelengths with the Atacama Large Millimeter/submillimeter Array (ALMA). Most of these discs are axisymmetric, with some also containing rings and gaps (ALMA Partnership et al. 2015; Andrews et al. 2016; Fedele et al. 2018; Andrews et al. 2018; Huang et al. 2018a; Dipierro et al. 2018; Booth & Ilee 2020), even though some of them are quite young ( $<1$  Myr). Ring and gap structures have also been observed in even younger ( $\lesssim 0.5$  Myr) Class 1 discs (Sheehan & Eisner 2018; Segura-Cox et al. 2020). Young discs are thought to be massive and could potentially be gravitationally unstable. A characteristic feature of such discs are large-scale spiral features. There is evidence that discs with spiral arms in the midplane exist (Pérez et al. 2016; Huang et al. 2018b), although they seem to be quite rare.

Does the lack of observed large-scale spiral structures imply that young discs are not as massive as expected? Or can signatures of gravitational instabilities be hidden? It is reasonable to assume that gravitationally unstable discs do not evolve in isolation. The physical processes that are often used to explain observed substructures such as rings and gaps, along with the mechanisms that can warp a disk, will also influence the evolution of young self-gravitating discs. A common explanation for rings and gaps are planet–disk interactions, which can also suppress spiral structures in gravitationally unstable discs (Rowther et al. 2020).

There are several mechanisms that can warp a protoplanetary disk. These include a misaligned internal (planetary or stellar) companion, a misaligned unbound stellar companion (flyby), or misaligned infalling material from chaotic accretion episodes. The rate at which these discs are observed also suggests that warps and misalignments are common in protoplanetary discs (Benisty et al. 2017; Walsh et al. 2017; Casassus et al. 2018;

Ballabio et al. 2021). The latter two mechanisms are more relevant for gravitationally unstable discs. Flybys are much more common earlier in a disk’s lifetime and become less frequent over time (Pfalzner 2013; Vincke & Pfalzner 2016; Bate 2018). Misaligned infall is also expected to occur very early in a disk’s lifetime when there is still plenty of material around the protostar (Bate 2018; Sakai et al. 2019). Both of these mechanisms are more likely to occur precisely when discs are more likely to be gravitationally unstable and can alter the evolution of the disk.

There have been some simulations of flybys interacting with a gravitationally unstable disk, but in these studies the flybys were coplanar or head-on. Additionally, the distance of closest approach occurred inside the disk causing major disruption to the disk structure and completely suppressing gravitational instabilities (Lodato et al. 2007; Forgan & Rice 2009). These works demonstrate that a flyby altering the disk structure can affect the heating and thus the self-gravitating structures. However, they do not consider warps or misalignments. Thies et al. (2010), on the other hand, did study the impact of inclined flybys and found that stellar encounters induced fragmentation. However, their disk masses were much more massive and hence more prone to fragmentation.

In this paper we use three-dimensional global numerical simulations to consider the evolution of an isolated self-gravitating disk subjected to a warp. To our knowledge, this is the first study of a self-gravitating disk subjected to a warp. This paper is organized as follows. In Section 2 we recall the relevant warp theory and its context in self-gravitating discs. In Section 3 we describe the simulations presented in this work. In Section 4 we present our results of the impact that an artificially introduced warp has on the structure and evolution of gravitationally unstable protoplanetary discs. We discuss our work in the context of its limitations and observations in Section 5. We conclude our work in Section 6.

## 2. Warp Theory

Warped discs are characterized by a radial dependence on the angular momentum vector. The steepness of the warp is



Original content from this work may be used under the terms of the [Creative Commons Attribution 4.0 licence](#). Any further distribution of this work must maintain attribution to the author(s) and the title of the work, journal citation and DOI.

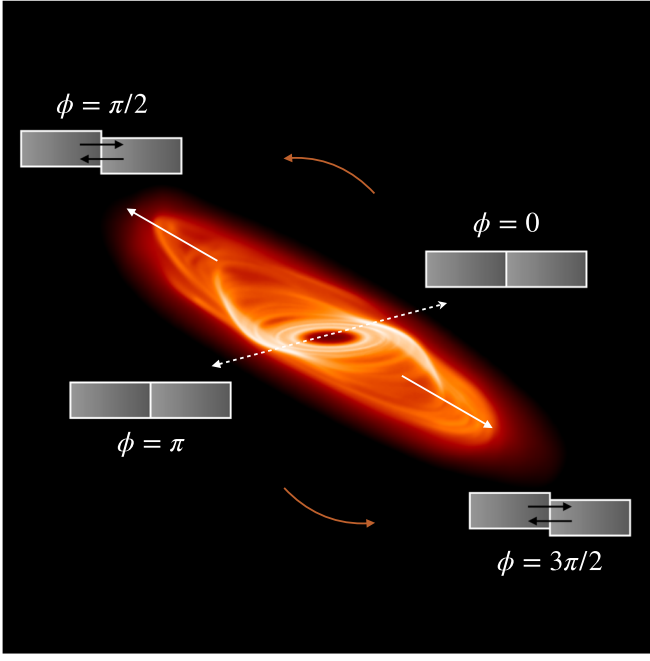


**Figure 1.** A three-dimensional projection of the disk after it has been warped. The annotations (see Figure 10 of Lodato & Pringle 2007) show the radial pressure gradients induced by the warp at different azimuths as a fluid element orbits the disk. The orange arrows show the rotation of the disk. The shaded gray boxes represent the pressure between adjacent annuli of gas. At  $\phi = 0$  and  $\phi = \pi$  the annuli are aligned, hence there is no pressure gradient. At all other azimuths, the heights of the annuli are offset resulting in an oscillating radial pressure gradient as the gas traverses an orbit. The direction of the resulting pressure gradient is shown by the black arrows. The color scale represents the surface density of the disk with brighter colors corresponding to regions of higher density.

described by the warp amplitude,  $\psi$ , which is given by (e.g., Lodato & Price 2010)

$$\psi = R \left| \frac{\partial \mathbf{l}}{\partial R} \right|, \quad (1)$$

where  $\mathbf{l}$  is the unit angular momentum vector, and  $R$  is the radial location spherical coordinates.

To demonstrate the effect that the warp has on the disk, in Figure 1 we show a three-dimensional projection of a warped gravitationally unstable disk with annotations to illustrate how the warp propagates through the disk. Consider a fluid element as it orbits around the disk with a position given by  $\phi$ . Here the disk may be described as concentric rings or annuli of gas and the warp causes adjacent rings to be vertically offset. The rotation of the disk is represented by the orange arrows. The shaded gray boxes represent the pressure between adjacent annuli of gas. At  $\phi = 0$  and  $\pi$ , adjacent rings will be perfectly aligned with no variation in the vertical height,  $z$ , hence at these locations there is no pressure gradient. At all other azimuths, adjacent rings will have variations in  $z$ , resulting in pressure gradients due to overpressure regions above or below the local midplane. The magnitude of the induced pressure gradient is given by (Lodato & Pringle 2007)

$$\frac{\partial P}{\partial R} \sim \frac{\partial P}{\partial z} \psi \sim \frac{P\psi}{H}, \quad (2)$$

where  $P$  is the pressure,  $z$  is the vertical height, and  $H$  is the disk scale height. The direction of the resulting pressure gradient, represented by the black arrows, changes based on

whether the fluid element is flowing toward or away from misaligned regions. As it moves toward vertically offset regions, away from  $\phi = 0$  and  $\pi$ , the resulting radial pressure gradient points inwards. The direction of the pressure gradient is reversed when flowing away from the vertically offset regions, toward  $\phi = 0$  and  $\pi$ . Hence the fluid element feels an oscillating pressure gradient as it orbits in the warp, which will drive the disk's evolution. This oscillating radial pressure gradient can trigger a strong response in the velocity flow in the disk. The response, for example in the radial velocity field from Lodato & Pringle (2007),

$$v_R \propto \psi \cos \phi, \quad (3)$$

depends on the warp amplitude of the disk and the azimuthal angle  $\phi$ .

In typical studies of warped protoplanetary discs, the equation of state is assumed to be isothermal, where  $PdV$  work is neglected (Lodato & Price 2010). However, in the work presented here where we consider warps in gravitationally unstable discs, which contains large-scale spiral structures that cause shocks,  $PdV$  work is naturally important. Hence, if a warp can excite strong responses in the velocity flow, the spiral structures in the disk are expected to be impacted due to additional  $PdV$  heating.

### 3. Method

#### 3.1. Hydrodynamical Simulations & Initial Conditions

We use PHANTOM, a smoothed-particle hydrodynamics (SPH) code developed by Price et al. (2018), to perform the suite of simulations presented here.

The disk is modeled using 2 million particles between  $R_{\text{in}} = 3$  and  $R_{\text{out}} = 150$  in code units with a disk-to-star mass ratio of 0.1. The central star is modeled using a fixed external potential. The initial surface mass density is set as a smoothed power law and is given by

$$\Sigma = \Sigma_{\text{in}} \left( \frac{R}{R_{\text{in}}} \right)^{-1} f_s, \quad (4)$$

where  $\Sigma_{\text{in}}$  is the surface mass density at  $R = R_{\text{in}}$  and  $f_s = 1 - \sqrt{R_{\text{in}}/R}$  is the factor used to smooth the surface density at the inner boundary of the disk. The initial temperature profile is expressed as a power law

$$T = T_{\text{in}} \left( \frac{R}{R_{\text{in}}} \right)^{-0.5}, \quad (5)$$

where  $T_{\text{in}}$  is set such that the disk aspect ratio  $H/R = 0.05$  at  $R = R_{\text{in}}$ . The internal energy equation is

$$\frac{du}{dt} = -\frac{P}{\rho} (\nabla \cdot \mathbf{v}) + \Lambda_{\text{shock}} - \frac{\Lambda_{\text{cool}}}{\rho}, \quad (6)$$

where we assume an adiabatic equation of state, and  $u$  is the specific internal energy. The first term on the RHS is the  $PdV$  work,  $\Lambda_{\text{shock}}$  is a heating term that is due to the artificial viscosity used to correctly deal with shock fronts, and

$$\Lambda_{\text{cool}} = \frac{\rho u}{t_{\text{cool}}} \quad (7)$$

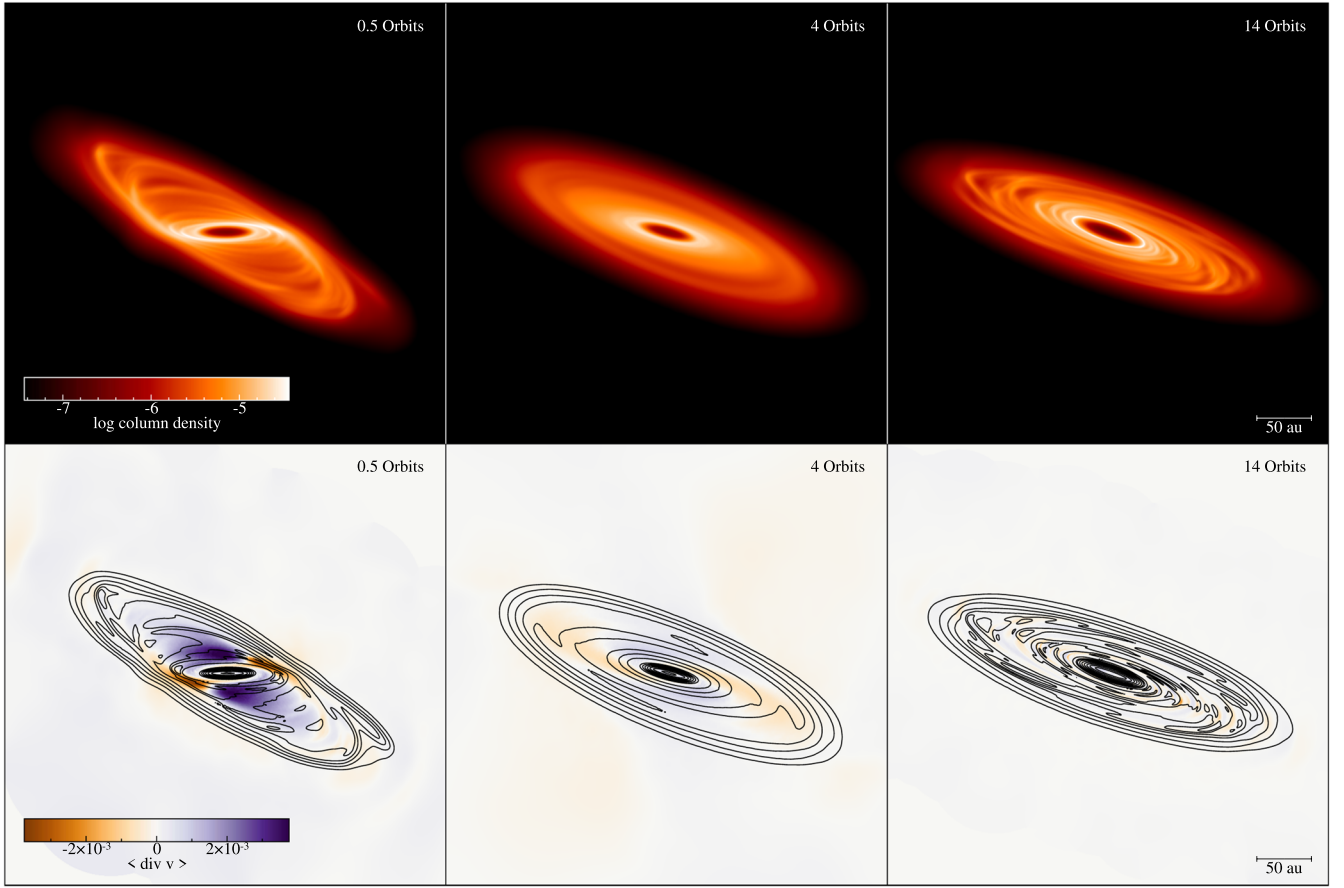


**Figure 2.** Plots of the surface density,  $\Sigma$  (top) and divergence of velocity,  $\nabla \cdot \mathbf{v}$  (bottom) in code units where the angled brackets represent a density weighted average, showing the evolution of a  $0.1 M_{\odot}$  disk 0.5, 4, and 14 orbits (from left to right) after a warp is introduced. The warp induces a strong response in the velocity flow of the disk (left panels), which heats it up resulting in an axisymmetric gravitationally stable disk (middle panels). After the disk has realigned, cooling takes over, with the disk eventually recovering its spiral features (right panels).

controls the cooling in the disk. Here, the cooling time is modeled using a simple prescription such that it is proportional to the dynamic time by a constant factor  $\beta_{\text{cool}}$  (Gammie 2001),

$$t_{\text{cool}} = \beta_{\text{cool}} \Omega^{-1}, \quad (8)$$

where  $\Omega$  is the orbital frequency. Assuming the transfer of angular momentum is locally driven by gravitoturbulence (Gammie 2001),  $\beta_{\text{cool}}$  can be related to the  $\alpha$  viscosity by (Shakura & Sunyaev 1973):

$$\alpha = \frac{4}{9} \frac{1}{\gamma(\gamma - 1)} \frac{1}{\beta_{\text{cool}}}. \quad (9)$$

Here  $\beta_{\text{cool}} = 15$ , which using the above equation gives a theoretical  $\alpha = 0.027$ . To model shocks, we use an artificial viscosity switch that utilizes the time derivative of the velocity divergence introduced by Cullen & Dehnen (2010). The artificial viscosity parameter,  $\alpha_v$ , varies depending on the proximity to a shock. It takes a maximum of  $\alpha_{\text{max}} = 1$  close to the shock and a minimum of  $\alpha_{\text{min}} = 0$  far away. The artificial viscosity coefficient,  $\beta_v$ , is set to 2 (see Price et al. 2018; Nealon et al. 2015).

### 3.2. Warping the Disk

Before the disk is warped, it is evolved for 10 orbits to allow it to become gravitationally unstable and develop spiral

structures. A warped disk can be described by two angles, its tilt,  $\beta$ , and its twist,  $\gamma$ . Using this, the unit angular momentum vector can be written as (Pringle 1996)

$$\mathbf{l} = (\cos \gamma \sin \beta, \sin \gamma \sin \beta, \cos \beta), \quad (10)$$

where the disk is considered warped if  $\mathbf{l}$  varies with radius. To introduce a warp in our simulation, the position of each particle is rotated such that the unit vector of the angular momentum is given by (Lodato & Price 2010)

$$l_x = \begin{cases} 0 & \text{for } R < R_1 \\ \frac{A}{2} \left[ 1 + \sin \left( \pi \frac{R - R_0}{R_2 - R_1} \right) \right] & \text{for } R_1 < R < R_2 \\ A & \text{for } R > R_2 \end{cases}$$

$$l_y = 0,$$

$$l_z = \sqrt{1 - l_x^2}, \quad (11)$$

where in our fiducial setup the warp is centered at  $R_0 = 75$  and extends from  $R_1 = 45$  to  $R_2 = 105$  in code units. The initial misalignment between the outer and inner disk,  $i = 30^\circ$ , defines  $A = \sin(i)$ . All disks in this work are initially untwisted since  $l_y = 0$ .

Figure 1 also helps to visualise how the warp profile affects the disk's evolution, as also described in Equations (2) and (3). For a steeper warp, i.e., a larger warp amplitude,  $\psi$ , a fluid

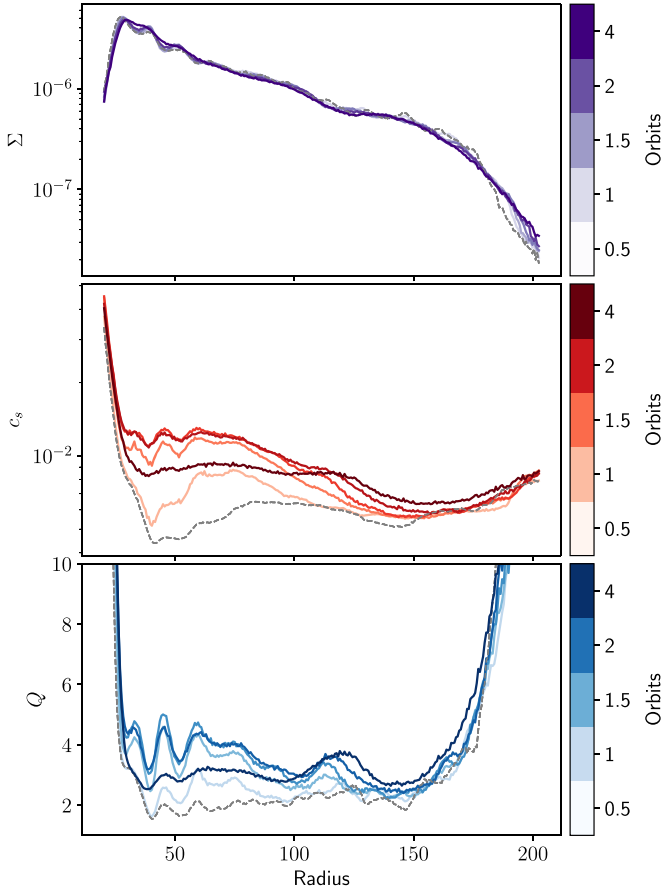


**Figure 3.** Azimuthally averaged surface density,  $\Sigma$  (top), the sound speed,  $c_s$  (middle), and the Toomre parameter,  $Q$  (top) in code units at 0.5, 1, 1.5, 2, and 4 orbits after the warp has been introduced. The darker shades represent later times. The dashed gray line in each panel is the initial profile at the moment the warp is introduced. The increase in  $c_s$  due to the warp is the reason for the increase in  $Q$  causing the disk to become gravitationally stable.

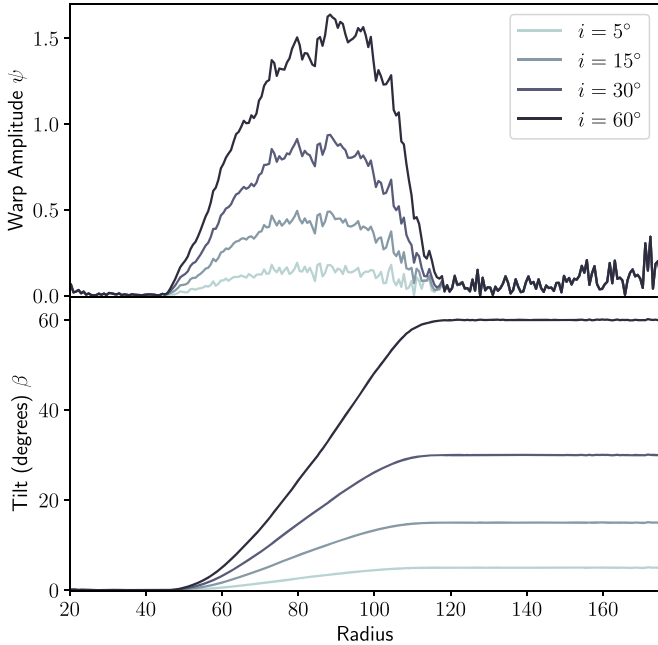


**Figure 4.** The warp amplitude,  $\psi$  (top), and the tilt,  $\beta$  (bottom), for the simulations where the initial disk misalignment,  $i$ , varies from  $5^\circ$  to  $60^\circ$ . The darker lines represent larger  $i$ . A larger initial disk misalignment results in a steeper tilt profile, and thus a larger warp amplitude.

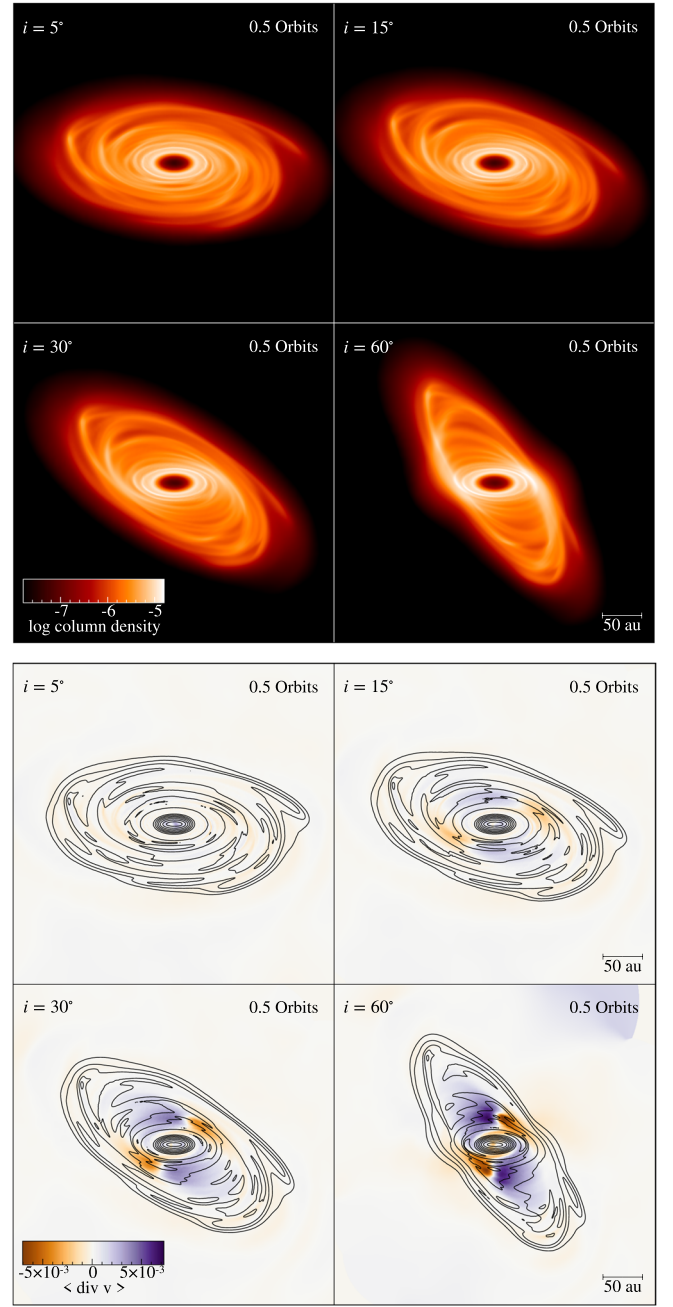


**Figure 5.** The surface density,  $\Sigma$  (top), and divergence of velocity,  $\nabla \cdot \mathbf{v}$  (bottom), in code units where the angled brackets represent a density weighted average, showing the evolution of a  $0.1 M_\odot$  disk 0.5 orbits after a warp has been introduced. The subplots are for a disk with initial misalignments of  $i = 5^\circ, 15^\circ, 30^\circ$ , and  $60^\circ$ . The  $\nabla \cdot \mathbf{v}$  plots show that the strength of the response to the velocity flow of the disk due to the warp is greater for larger  $i$ .

element will experience a larger pressure gradient from adjacent rings as it orbits around the disk. Hence to investigate the importance of the warp amplitude  $\psi$  on the disk evolution, we consider multiple simulations. First, we consider various inclinations where simulations are performed with  $i = 5^\circ, 15^\circ$ , and  $60^\circ$ . By changing only the initial disk misalignment, the only difference to the fiducial setup is the maximum value of  $\psi$ . Second, the impact of the warp location is also investigated with two additional simulations with the same warp width ( $R_2 - R_1 = 60$ ) and initial disk misalignment ( $i = 30^\circ$ ), but at  $R_0 = 50$  and  $100$ .



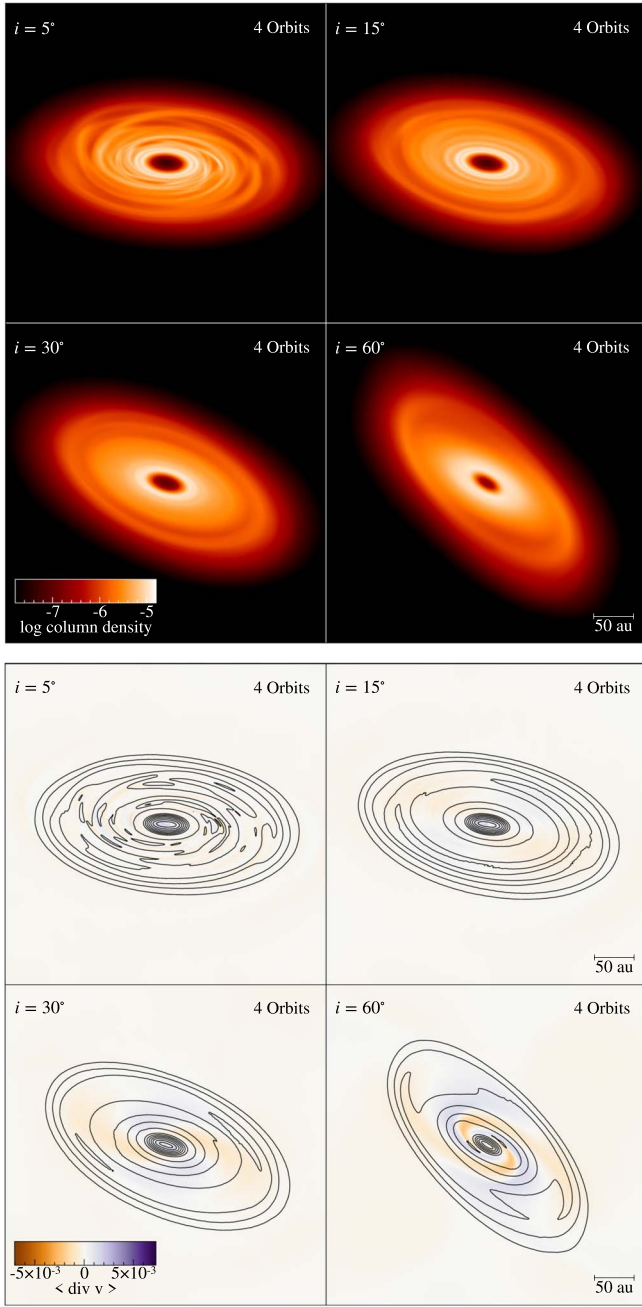


**Figure 6.** Same as Figure 5, but at 4 orbits after the warp has been introduced. Due to the strong response to the velocity flow, the discs in the bottom row ( $i = 30^\circ$  and  $60^\circ$ ) have heated up enough to become gravitationally stable and lose their spiral structures. Whereas for a slight misalignment ( $i = 5^\circ$ ), the spiral structures are unaffected as the disk has experienced negligible heating.

## 4. Results

### 4.1. Evolution Into a Gravitationally Stable Disk

As the disk in our fiducial simulation evolves, the warp propagates radially both inwards and outwards. The influence of the warp quickly suppresses the spiral structures yielding an axisymmetric gravitationally stable disk. Since the warp is not maintained by external forces, as the disk continues to evolve, the warp smooths out and the disk becomes coplanar. The top panels of Figure 2 shows the surface density of the disk at three snapshots at 0.5, 4, and 14 orbits after the disk is warped. The leftmost panels show the disk in the early stages when it is still

warped. The middle panels show the disk while the warp is dissipating at  $t = 4$  orbits. Here, the disk is smooth with no signs of any spiral structures left. The rightmost panels show the disk much later in its evolution after the warp has completely dissipated at  $t = 14$  orbits. Due to the constant  $\beta_{\text{cool}}$  used to cool the disk, the disk cools back down and becomes gravitationally unstable once more after the warp has dissipated and the disk is back to being flat.

To demonstrate what drives the disk to become gravitationally stable, the azimuthally averaged surface density,  $\Sigma$ , sound speed,  $c_s$ , and Toomre  $Q$  parameter (Toomre 1964) are plotted in Figure 3, where the darker lines represent later times. The Toomre parameter is given by

$$Q = \frac{c_s \Omega}{\pi G \Sigma}. \quad (12)$$

Protoplanetary discs are considered to be gravitationally unstable when spiral structures form. The critical value to form nonaxisymmetric instabilities such as spiral arms is when  $Q \lesssim 1.7$  (Durisen et al. 2007). We see that the surface density of the disk is mostly unchanged once the warp is introduced. However, as seen by the increase in  $c_s$ , the influence of the warp heats up the disk by enough to put it in the gravitationally stable regime. During the first couple of orbits when the disk is still warped, Figure 3 shows that the disk continues to heat up. As the warp dissipates as the disk evolves, cooling takes over and the disk starts to cool back down. Due to the simple cooling prescription, the inner regions of the disk begin to cool down first. This is expected in a disk cooled with a constant  $\beta_{\text{cool}}$ , where the disk cools faster in the inner disk. Eventually the warp has dissipated such that the disk can cool down enough to reform its spiral structures. The rightmost panels in Figure 2 show the disk at 14 orbits when it is gravitationally unstable again.

To determine why the disk initially heats up, we investigate the role of  $PdV$  work. The bottom panel in Figure 2 shows  $\nabla \cdot \mathbf{v}$ , the divergence of the velocity. Recalling from Section 2 that the warp induces a response in the radial velocity, we examine the consequence of this on the heating in the disk. As the divergence of the velocity directly contributes to the energy (and thus temperature) of the disk (see Equation (6)), we can use  $\nabla \cdot \mathbf{v}$  as a proxy for the heating due to  $PdV$  work that is occurring in the disk. In the early stages of evolution at 0.5 orbits, the disk is still warped. As mentioned in Section 2, strong radial pressure gradients are induced due to adjacent annuli of gas varying with vertical height  $z$ . This triggers a response in the induced radial velocity of the disk that heats it up, as seen by the large magnitude of  $\nabla \cdot \mathbf{v}$  in the bottom-left panel of Figure 2. As the disk evolves, the warp dissipates as there is no external torque sustaining the warp. At 4 orbits, the disk is nearly flat and hence there is little variance in the pressure gradient. Thus, the magnitude of  $\nabla \cdot \mathbf{v}$  has greatly decreased, as expected, leading to less heating from  $PdV$  work. At 14 orbits, the only contributions to  $PdV$  heating is due to the gravitational instabilities in the disk, which are much weaker compared to the  $PdV$  work due to the warp.

### 4.2. Impact of Warp Inclination

Figure 4 shows the initial warp profile for three additional simulations, each with a different initial disk misalignment of

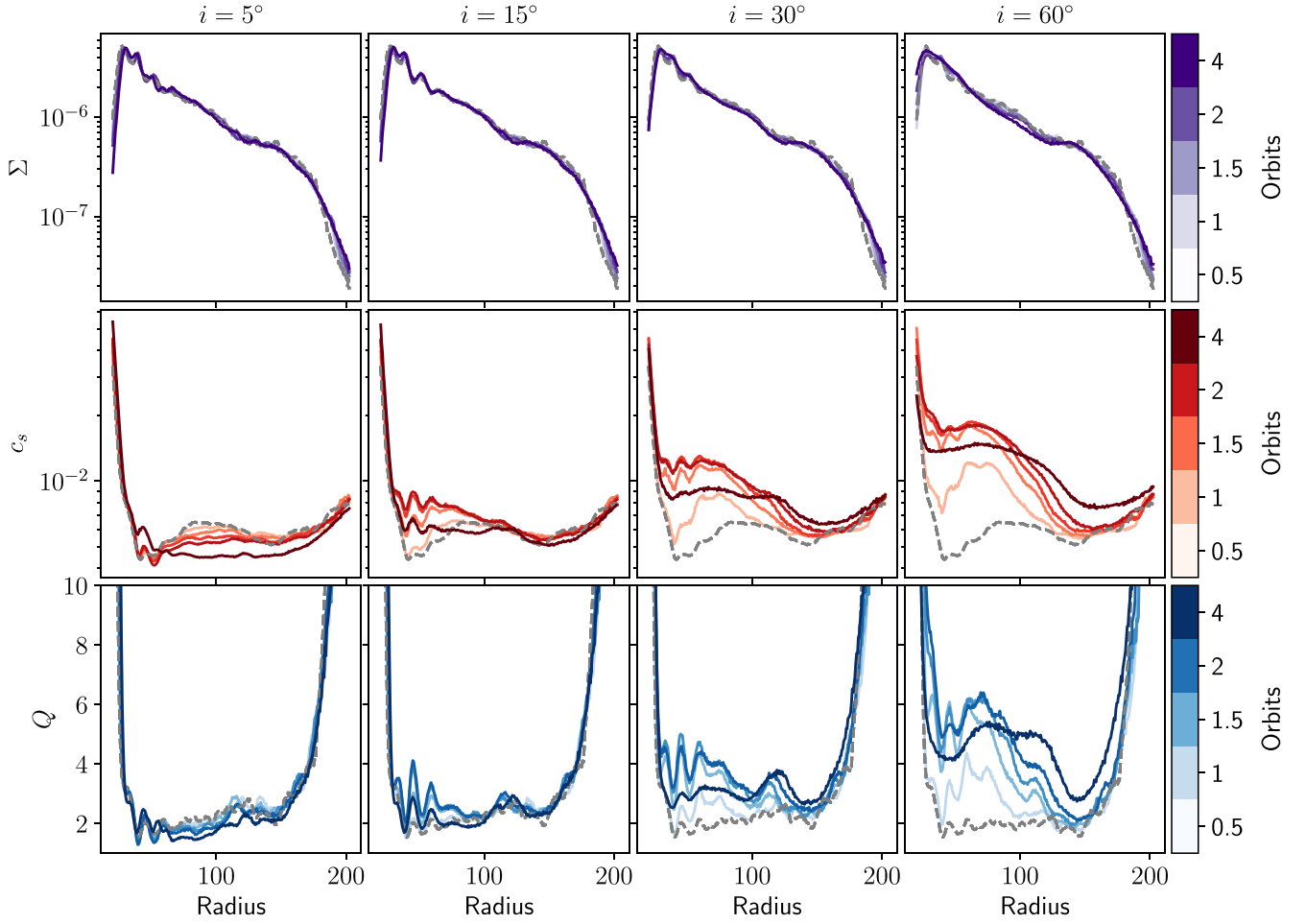


**Figure 7.** The azimuthally averaged surface density,  $\Sigma$  (top panels), sound speed,  $c_s$  (middle panels), and Toomre  $Q$  parameter (bottom panels) in code units for the discs with initial disk misalignment  $i = 5^\circ$ ,  $15^\circ$ ,  $30^\circ$ , and  $60^\circ$  (from left to right). The darker shades represent later times. The dashed line represents the conditions at  $t = 0$ . The disk only experiences sufficient heating to become gravitationally stable when  $i = 30^\circ$  and  $60^\circ$ .

$i = 5^\circ$ ,  $15^\circ$ , and  $60^\circ$  to compare with the fiducial simulation with  $i = 30^\circ$ . Recalling Equation 2, the pressure gradient induced by the warp depends on the pressure,  $p$ , disk scale height,  $H$ , and warp amplitude,  $\psi$ . By fixing  $R_0$  and  $R_2 - R_1$ , the location and extent of the warp, respectively,  $p$  and  $H$  are unchanged in the warped regions for all four discs. Thus, only changing the maximum value of  $\psi$  allows for easier comparison of how the warp affects the evolution of the disk.

Figures 5 and 6 show the surface density and the divergence of the velocity at 0.5 and 4 orbits, respectively, after the warp has been introduced. From the plots of  $\nabla \cdot \mathbf{v}$  in Figure 5 it is clear that, all else being equal, the discs with the stronger warp profiles trigger greater responses in the induced radial velocity of the disk. This is easiest seen comparing the two extremes where  $i = 5^\circ$  and  $i = 60^\circ$  (top-left and bottom-right subpanels). For the disk where  $i = 5^\circ$ , there is little change to the  $\nabla \cdot \mathbf{v}$  of the disk, whereas with  $i = 60^\circ$ , there is a large impact on  $\nabla \cdot \mathbf{v}$  throughout most of the disk. Figure 6 shows the consequence of the warp on the disk structure. It can be seen that the discs with stronger misalignments ( $i = 30^\circ$  and  $i = 60^\circ$ , in particular), which trigger stronger responses in the induced radial velocity of the disk, experience greater heating resulting in the discs becoming gravitationally stable with no signs of spiral structures after a few orbits.

This is reflected in Figure 7, which shows the azimuthally averaged surface density,  $\Sigma$  (top panels), sound speed,  $c_s$ ,

(middle panels), and Toomre  $Q$  parameter (bottom panels). In all cases, the surface density is mostly unchanged as with the fiducial case. The change in the sound speed, on the other hand, has a strong dependence on the initial disk misalignment. In general, a larger initial disk misalignment, and hence a larger warp amplitude  $\psi$ , results in more heating. However, simply having a misaligned disk does not necessarily result in the disk becoming gravitationally stable. With a slight misalignment of  $i = 5^\circ$ , since there is very little change to the velocity flow of the disk, the contribution to the  $PdV$  work due to the warp is negligible, and the disk simply continues to cool as expected due to the constant  $\beta_{\text{cool}}$  used in these simulations. Although there is some heating in the  $i = 15^\circ$  case, it is not enough to push the disk into the gravitationally stable regime as it quickly cools back down to prewarp levels. It is only in the  $i = 30^\circ$  and  $60^\circ$  cases that there is enough heating to result in the disk becoming completely gravitationally stable.

#### 4.3. Impact of Warp Location

Unlike in Section 4.2 where varying the initial disk misalignment,  $i$ , only changes the warp profile, varying the warp location,  $R_0$ , adds additional complexities to the evolution of a warped disk. Figure 8 shows the warp profiles (first two panels), the initial pressure,  $p$  (third panel), and disk scale height,  $H$  (bottom panel), for the simulations with  $R_0 = 50, 75$ ,

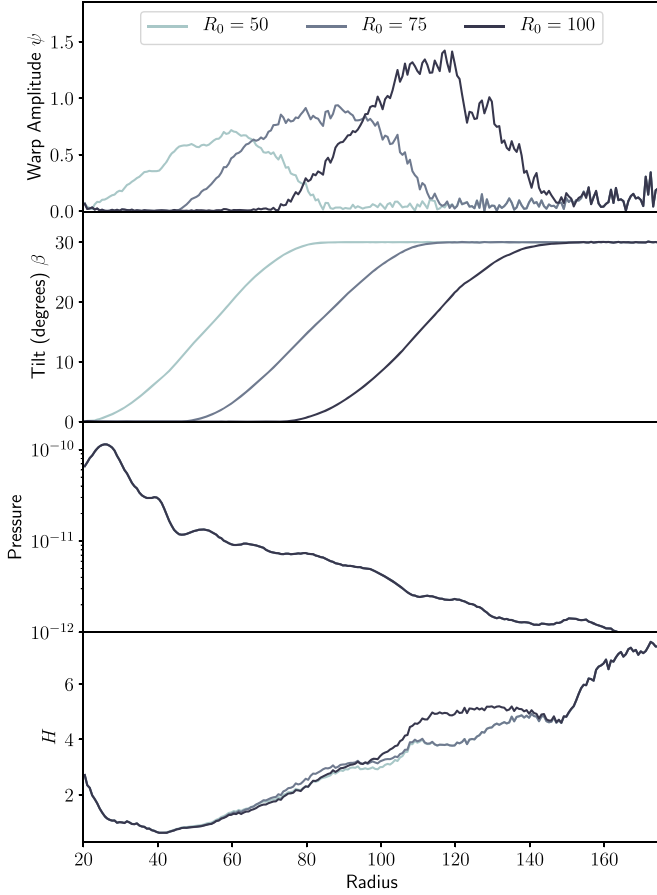


**Figure 8.** The warp amplitude,  $\psi$  (first panel), and the tilt,  $\beta$  (second panel), for the simulations where the warp location,  $R_0 = 50, 75$ , and  $100$ . The darker lines represent larger  $R_0$ . The maximum value of  $\psi$  increases at higher  $R_0$ . The pressure and disk scale height in code units are shown in the third and fourth panels, respectively. The pressure profile is the same for all simulations, hence the lines are coincident.

and  $100$ . The bottom two panels are important to understanding the pressure gradients induced by the warp, recalling Equation 2.

Since the warp amplitude,  $\psi$ , is larger for increasing  $R_0$ , based on the results in Section 4.2 we might naïvely expect the magnitude of  $\nabla \cdot \mathbf{v}$  to be largest for the disk warped at  $R_0 = 100$ . However, from Figure 9 this is clearly not the case. Instead, the largest change to  $\nabla \cdot \mathbf{v}$  is for the disk warped at  $R_0 = 50$ , which has the smallest  $\psi$ . To reconcile this discrepancy, we have to also consider the pressure and scale height at each  $R_0$ . From Figure 8, the pressure increases while the disk scale height decreases for smaller  $R_0$ . Both of these work toward increasing the pressure gradients induced by the warp (see Equation (2)), thus triggering a stronger response in  $\nabla \cdot \mathbf{v}$  for smaller  $R_0$ , which is consistent with our results.

Based on the results in Section 4.2 we should expect the spiral structures to be most weakened for the discs warped at smaller  $R_0$ , since they have the largest change in  $\nabla \cdot \mathbf{v}$ . However, from Figure 10, this is clearly not the case. Instead, the impact to the disk structure is greater at larger  $R_0$ . To understand why, we have to now consider the timescale at which warp propagation is damped,  $t_{\text{damp}} = (\alpha\Omega)^{-1}$  (Lubow & Ogilvie 2000), and the cooling timescale,  $t_{\text{cool}} = \beta_{\text{cool}}\Omega^{-1}$  (Gammie 2001). Both of these timescales are longer at larger  $R_0$ . A longer  $t_{\text{damp}}$  results in the disk taking longer to realign.

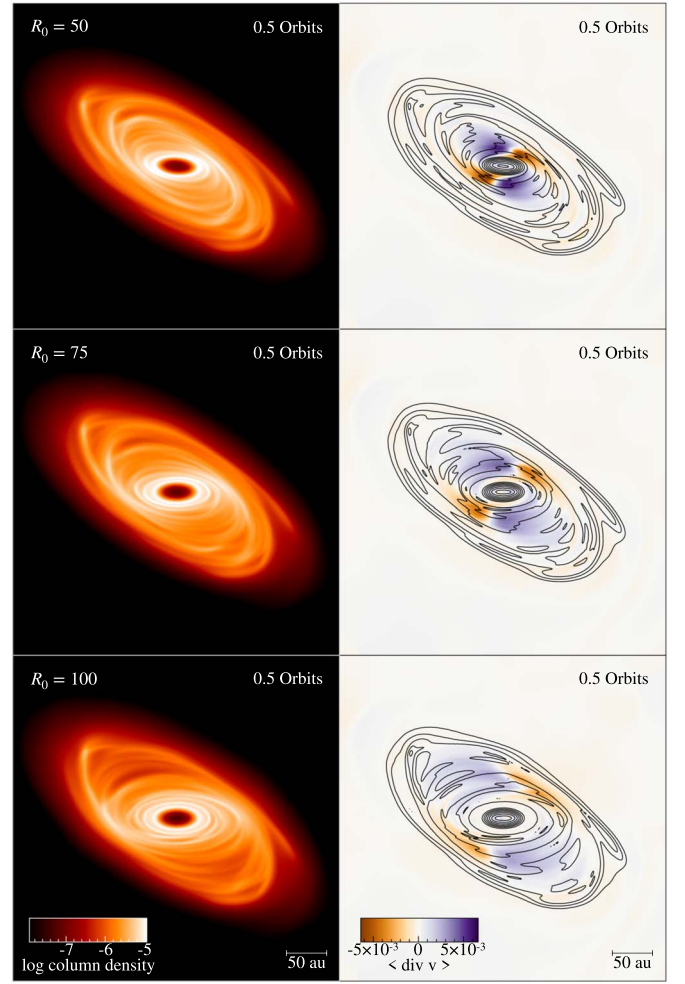


**Figure 9.** The surface density,  $\Sigma$  (left), and divergence of velocity,  $\nabla \cdot \mathbf{v}$  (right), in code units showing the evolution of a  $0.1 M_\odot$  disk 0.5 orbits after a warp has been introduced. The subplots are for a disk with the warp located at  $R_0 = 50, 75$ , and  $100$ . Although the warp amplitude,  $\psi$ , increases with higher  $R_0$ , the magnitude of  $\nabla \cdot \mathbf{v}$  is largest at lower  $R_0$ , which is at odds with the results in Figure 5. However, once the differences in pressure,  $p$ , and disk scale height,  $H$ , at different  $R_0$  are considered, this discrepancy is reconciled. Higher pressures and a smaller scale height at lower  $R_0$  counter the lower warp amplitude giving rise to greater response in the induced radial velocity.

Since the disk is in a warped state for an increased duration, the heating due to the warp is prolonged. Comparing the right panels of Figures 9 and 10 shows that the magnitude of  $\nabla \cdot \mathbf{v}$  has decreased the most for  $R_0 = 50$ , whereas for  $R_0 = 100$  the magnitude of  $\nabla \cdot \mathbf{v}$  has not changed too much. This is consistent with the disk realigning much faster for a warp at  $R_0 = 50$ . Since  $t_{\text{cool}}$  is also shorter at smaller  $R_0$ , cooling is faster in the inner regions of the disk due to the simple cooling model used. Hence, the heating due to the warp is less efficient for smaller  $R_0$ .

Figure 11 shows the azimuthally averaged surface density,  $\Sigma$  (top panels), sound speed,  $c_s$  (middle panels), and Toomre  $Q$  parameter (bottom panels) for these simulations. The impact of the shorter cooling and realignment timescales at smaller  $R_0$  is more apparent in this figure. The disk with  $R_0 = 50$  cools the quickest. Additionally, since the disk also realigns the fastest for  $R_0 = 50$ , the heating due to the warp does not last long enough to spread throughout the disk. This is in contrast to the disk with  $R_0 = 100$ , which has experienced the most heating globally due to a longer realignment timescale. In general, we



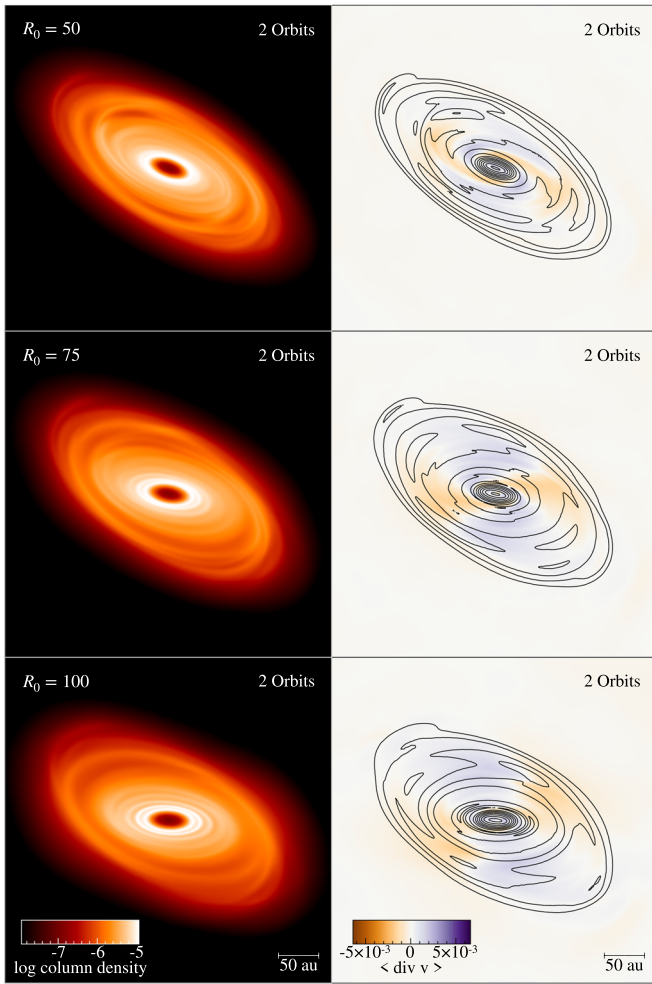


**Figure 10.** Same as Figure 9 but at 2 orbits after the warp has been introduced. Despite the magnitude of  $\nabla \cdot \mathbf{v}$  being initially larger at lower  $R_0$ , the impact to the spiral structures is greater at larger  $R_0$ . This result initially appears at odds with Figure 6, where the spiral structures are most suppressed with increasing magnitudes of  $\nabla \cdot \mathbf{v}$ . However, consideration of the cooling and realignment timescales reconciles this discrepancy. Both timescales are shorter at smaller  $R_0$ . Hence, we expect the magnitude of  $\nabla \cdot \mathbf{v}$ , and hence the amount of heating, to decrease faster for discs warped at lower  $R_0$ , which can be seen by comparing with the right panels of Figure 9 to see how much the magnitude of  $\nabla \cdot \mathbf{v}$  has changed by. Therefore, the results here are consistent with our expectations of spiral structures being most impacted at larger  $R_0$  since the heating due to the warp is prolonged and more efficient at larger  $R_0$ .

find that the spiral structures are more affected by a warp located further out, which results in the disk being heated up for a longer duration.

## 5. Discussion

### 5.1. Disk Cooling & Long-term Evolution

The cooling parameter,  $\beta_{\text{cool}}$  is constant both spatially and temporally. Although commonly used to model self-gravitating discs, comparison with radiative transfer models show that  $\beta_{\text{cool}}$  should vary in both time and space (Mercer et al. 2018). For the purposes of this work, a constant  $\beta_{\text{cool}}$  is justified as we are primarily interested in how the evolution of the disk structure responds to a warp. Since  $PdV$  heating dominates over cooling while the disk is warped, we expect the qualitative results to hold; a warp acts to move a self-gravitating disk toward stability.

However, the long-term evolution of the disk will be better understood when taking into account the non-coplanar geometry with more sophisticated disk thermodynamics. In all simulations where the disk becomes gravitationally stable due to the warp, the disk eventually cools back down to become gravitationally unstable and recover its spirals throughout the disk. This is simply a result of the cooling model, which is time independent and thus does not take into account the structural evolution of the disk. Additionally, the shorter cooling time in the inner disk naturally results in spiral structures forming more quickly in the inner regions, contrary to expectation of realistic self-gravitating discs (Rafikov 2005; Stamatellos & Whitworth 2009; Rice & Armitage 2009; Clarke 2009). Hence, more realistic thermodynamics are needed to better understand the longer-term evolution of the suppression of spiral structures due to the warp.

### 5.2. Formation of Rings & Gaps

An interesting result that could have important implications on observations is the formation of rings and gaps from the evolution of a warped gravitationally unstable disk. We find tentative evidence of ring and gap structure, most easily seen in the bottom row of Figures 6 ( $i = 30^\circ$  and  $60^\circ$ ) and 10 ( $R_0 = 100$ ). The evolution of the warp amplitude, which has a continuous decline in magnitude, combined with the surface density profiles suggests that the gap is not a result of disk breaking. We also do not expect the disk to break due to the high  $\alpha$  viscosities (Doğan et al. 2018) associated with gravitationally unstable discs generally and in our simulations ( $\alpha \sim 0.1$ ). Our results instead suggest that the spiral structures initially present in our disk evolved into ring and gap structure as a result of the warp propagation. However, the morphology of the spiral structures depend on the disk thermodynamics. Thus, more detailed simulations are required to determine if warps in gravitationally unstable discs can explain some of the substructures seen in observations. This may explain features in existing discs such as Elias 2-27, which contains a gap, spiral structures, and evidence of a warp (Paneque-Carreno et al. 2021). If the warp in Elias 2-27 is located in the inner parts of the disk, the impact of the warp could be localised to the inner disk allowing the spiral structures in the outer regions of the disk to survive.

## 6. Conclusion

We perform three-dimensional SPH simulations to investigate the impact of a warp on the structure of a gravitationally unstable disk. Our work shows that if the warp is strong enough, it can suppress spiral structures due to gravitational instability. This is due to the oscillating radial pressure gradient induced by the warp, which triggers a response in the velocity flow of the disk. This causes the disk to heat up and become gravitationally stable. In some cases, the disk evolves to form a ring and gap structure, which could have important observational implications.

We find that that the structure is more impacted for warps with larger initial disk misalignments and for warps located further out. In the former case, a larger initial misalignment simply results in larger pressure gradients due to a larger warp amplitude, and thus a stronger response in the velocity flow of the disk leading to increased heating. The latter case is more complicated due to the physical properties of the disk varying



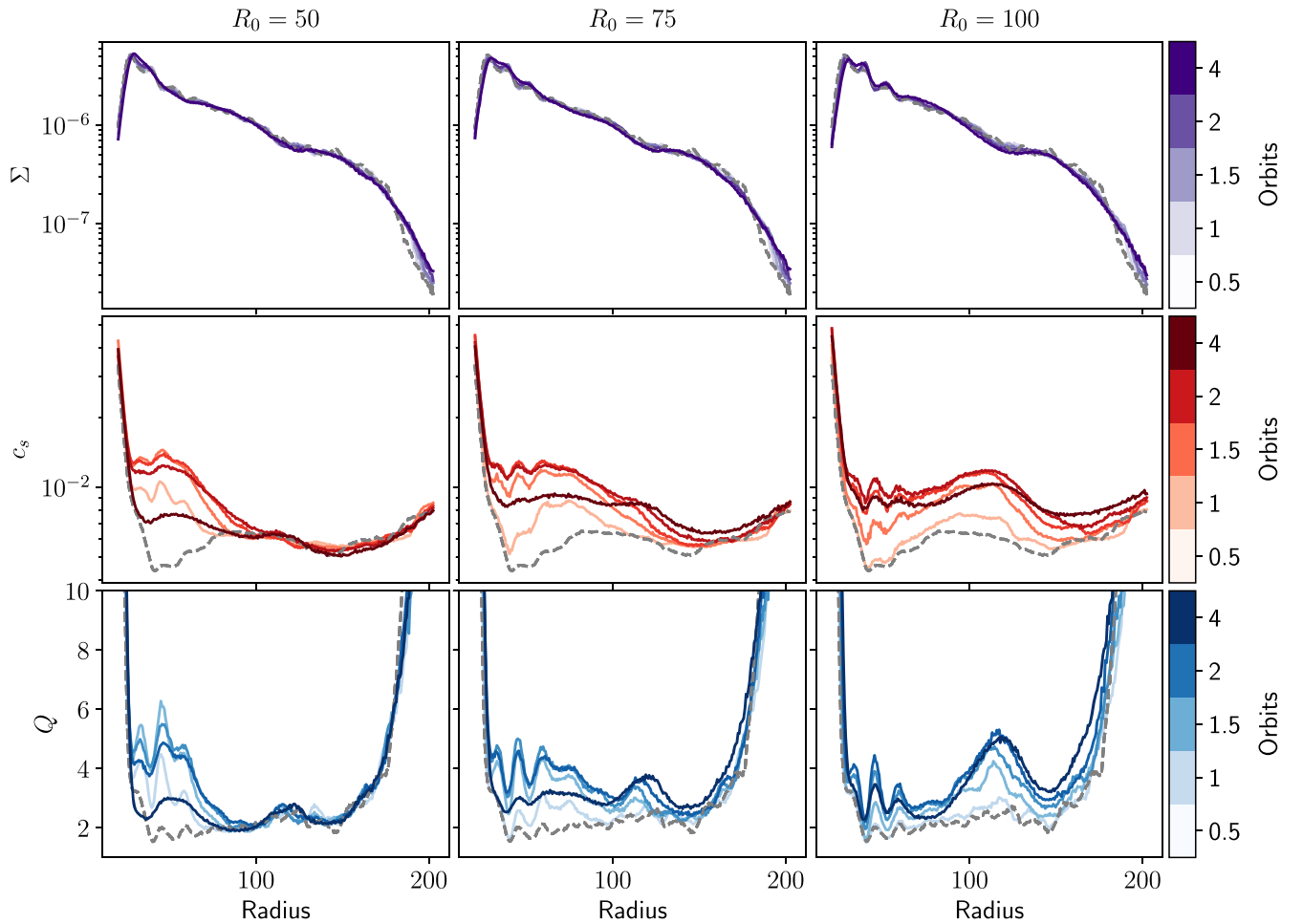


**Figure 11.** The azimuthally averaged surface density,  $\Sigma$  (top panels), sound speed,  $c_s$  (middle panels), and Toomre  $Q$  parameter (bottom panels) in code units for the discs with the warp located at  $R_0 = 50, 75$ , and  $100$  (from left to right). The darker shades represent later times. The dashed line represents the conditions at  $t = 0$ . The disk experiences greater heating, and thus is more impacted, at larger  $R_0$  due to longer cooling and realignment timescales at larger radii.

with radius, but a warp located further out has a greater impact on the spiral structure due to a longer realignment timescale, which results in prolonged heating. Finally, we note that a more detailed treatment of the disk thermodynamics is required to understand the long-term evolution of the tentative ring and gap structure we identify in some of our simulations.

We thank Giuseppe Lodato for useful discussions and the anonymous referee for their comments that benefited this work. S.R. acknowledges support from a Royal Society Enhancement Award. F.M. acknowledges support from the Royal Society Dorothy Hodgkin Fellowship. R.N. acknowledges support from UKRI/EPSC through a Stephen Hawking Fellowship (EP/T017287/1). This work was performed using Orac, the HPC cluster at the University of Warwick.

*Software:* Matplotlib (Hunter 2007), numpy (van der Walt et al. 2011), pandas (pandas development team 2020; McKinney 2010), PHANTOM (Price et al. 2018), SPLASH (Price 2007).

## ORCID iDs

Sahl Rowther <https://orcid.org/0000-0003-4249-4478>  
 Rebecca Nealon <https://orcid.org/0000-0003-0856-679X>  
 Farzana Meru <https://orcid.org/0000-0002-3984-9496>

## References

- ALMA Partnership, Brogan, C. L., Pérez, L. M., et al. 2015, *ApJL*, **808**, L3  
 Andrews, S. M., Huang, J., Pérez, L. M., et al. 2018, *ApJL*, **869**, L41  
 Andrews, S. M., Wilner, D. J., Zhu, Z., et al. 2016, *ApJL*, **820**, L40  
 Ballabio, G., Nealon, R., Alexander, R. D., et al. 2021, *MNRAS*, **504**, 888  
 Bate, M. R. 2018, *MNRAS*, **475**, 5618  
 Benisty, M., Stolker, T., Pohl, A., et al. 2017, *A&A*, **597**, A42  
 Booth, A. S., & Ilee, J. D. 2020, *MNRAS*, **493**, L108  
 Casassus, S., Avenhaus, H., Pérez, S., et al. 2018, *MNRAS*, **477**, 5104  
 Clarke, C. J. 2009, *MNRAS*, **396**, 1066  
 Cullen, L., & Dehnen, W. 2010, *MNRAS*, **408**, 669  
 Dipierro, G., Ricci, L., Pérez, L., et al. 2018, *MNRAS*, **475**, 5296  
 Doğan, S., Nixon, C. J., King, A. R., & Pringle, J. E. 2018, *MNRAS*, **476**, 1519  
 Durisen, R. H., Boss, A. P., Mayer, L., et al. 2007, in *Protostars and Planets V*, ed. B. Reipurth, D. Jewitt, & K. Keil (Tucson, AZ: Univ. Arizona Press), 607  
 Fedele, D., Tazzari, M., Booth, R., et al. 2018, *A&A*, **610**, A24  
 Forgan, D., & Rice, K. 2009, *MNRAS*, **400**, 2022  
 Gammie, C. F. 2001, *ApJ*, **553**, 174  
 Huang, J., Andrews, S. M., Dullemond, C. P., et al. 2018a, *ApJL*, **869**, L42  
 Huang, J., Andrews, S. M., Pérez, L. M., et al. 2018b, *ApJL*, **869**, L43  
 Hunter, J. D. 2007, *CSE*, **9**, 90  
 Lodato, G., Meru, F., Clarke, C. J., & Rice, W. K. M. 2007, *MNRAS*, **374**, 590  
 Lodato, G., & Price, D. J. 2010, *MNRAS*, **405**, 1212  
 Lodato, G., & Pringle, J. E. 2007, *MNRAS*, **381**, 1287  
 Lubow, S. H., & Ogilvie, G. I. 2000, *ApJ*, **538**, 326  
 McKinney, W. 2010, in *Proc. 9th Python in Science Conf.*, ed. Stéfan van der Walt & Jarrod Millman, 56  
 Mercer, A., Stamatellos, D., & Dunhill, A. 2018, *MNRAS*, **478**, 3478  
 Nealon, R., Price, D. J., & Nixon, C. J. 2015, *MNRAS*, **448**, 1526

- pandas development team, T. 2020, pandas-dev/pandas: Pandas v1.4.0rc0, Zenodo, doi:[10.5281/zenodo.3509134](https://doi.org/10.5281/zenodo.3509134)
- Paneque-Carreno, T., Perez, L. M., Benisty, M., et al. 2021, [ApJ](#), **914**, 88
- Pérez, L. M., Carpenter, J. M., Andrews, S. M., et al. 2016, [Sci](#), **353**, 1519
- Pfalzner, S. 2013, [A&A](#), **549**, A82
- Price, D. J. 2007, [PASA](#), **24**, 159
- Price, D. J., Wurster, J., Tricco, T. S., et al. 2018, [PASA](#), **35**, e031
- Pringle, J. E. 1996, [MNRAS](#), **281**, 357
- Rafikov, R. R. 2005, [ApJL](#), **621**, L69
- Rice, W. K. M., & Armitage, P. J. 2009, [MNRAS](#), **396**, 2228
- Rowther, S., Meru, F., Kennedy, G. M., Nealon, R., & Pinte, C. 2020, [ApJL](#), **904**, L18
- Sakai, N., Hanawa, T., Zhang, Y., et al. 2019, [Natur](#), **565**, 206
- Segura-Cox, D. M., Schmiedeke, A., Pineda, J. E., et al. 2020, [Natur](#), **586**, 228
- Shakura, N. I., & Sunyaev, R. A. 1973, [A&A](#), **24**, 337
- Sheehan, P. D., & Eisner, J. A. 2018, [ApJ](#), **857**, 18
- Stamatellos, D., & Whitworth, A. P. 2009, in AIP Conf. Ser. 1094, 15th Cambridge Workshop on Cool Stars, Stellar Systems, and the Sun, ed. E. Stempels (Melville, NY: AIP), 557
- Thies, I., Kroupa, P., Goodwin, S. P., Stamatellos, D., & Whitworth, A. P. 2010, [ApJ](#), **717**, 577
- Toomre, A. 1964, [ApJ](#), **139**, 1217
- van der Walt, S., Colbert, S. C., & Varoquaux, G. 2011, [CSE](#), **13**, 22
- Vincke, K., & Pfalzner, S. 2016, [ApJ](#), **828**, 48
- Walsh, C., Daley, C., Facchini, S., & Juhász, A. 2017, [A&A](#), **607**, A114